



Cite this: *Nanoscale*, 2015, **7**, 4995

Controlling the morphology, composition and crystal structure in gold-seeded $\text{GaAs}_{1-x}\text{Sb}_x$ nanowires[†]

Xiaoming Yuan,^{*a} Philippe Caroff,^{*a} Jennifer Wong-Leung,^{a,b} Hark Hoe Tan^a and Chennupati Jagadish^a

While III–V binary nanowires are now well controlled and their growth mechanisms reasonably well understood, growing ternary nanowires, including controlling their morphology, composition and crystal structure remains a challenge. However, understanding and control of ternary alloys is of fundamental interest and critical to enable a new class of nanowire devices. Here, we report on the progress in understanding the complex growth behaviour of gold-seeded $\text{GaAs}_{1-x}\text{Sb}_x$ nanowires grown by metalorganic vapour phase epitaxy. The competition between As and Sb atoms for incorporation into the growing crystal leads to a tunability of the Sb content over a broad range (x varies from 0.09 to 0.6), solely by changing the AsH_3 flow. In contrast, changing TMSb flow is more effective in affecting the morphology and crystal structure of the nanowires. Inclined faults are found in some of these nanowires and directly related to the kinking of the nanowires and controlled by TMSb flow. Combined with the observed sharp increase of wetting angle between the Au seed and nanowire, the formation of inclined faults are attributed to the Au seed being dislodged from the growth front to wet the sidewalls of the nanowires, and are related to the surfactant role of Sb. The insights provided by this study should benefit future device applications relying on taper- and twin-free ternary antimonide III–V nanowire alloys and their heterostructures.

Received 27th October 2014,
Accepted 8th February 2015

DOI: 10.1039/c4nr06307d
www.rsc.org/nanoscale

1. Introduction

III–V ternary nanowires (NWs) are attracting ever increasing attention because of the promises offered by their widely tunable bandgaps and associated bandgap engineering for a variety of optoelectronic applications.^{1–3} Despite the recent progress in growth and tunability of ternary III–V nanowire alloys,^{4–10} intermixing, segregation,^{11–13} atomic ordering⁹ and miscibility gap phenomena, resulting from the additional anion or cation and controlled by both nucleation kinetics and thermodynamics, complicate growth drastically. Critical challenges include axial^{13,14} and radial¹² composition non-uniformity observed in most reports.^{12–15} Even though self-induced composition inhomogeneities have been shown to be useful in some cases,^{11,16} most applications would require composition homogeneity. One of the main causes of inhomogeneity is related to concomitant axial (vapour liquid solid

(VLS)) and radial growth *via* vapour-solid (VS) mechanism on the sidewalls resulting in tapered NWs with unintentional formation of a core–shell structure.^{6,12} As a consequence, understanding of the growth mechanisms of ternary nanowires is crucial in reducing tapering and preserving a pure crystal phase.

Here we choose $\text{GaAs}_{1-x}\text{Sb}_x$ as a model system for ternary NWs with two anions (As and Sb). This alloy is of interest due to its promising applications in high speed optoelectronics, solar cells, infrared photodetectors and even fundamental studies of electron and hole transport when combined into heterostructures with standard III-(As,P) materials.^{17–21} Indeed, the bandgap of $\text{GaAs}_{1-x}\text{Sb}_x$ can be tuned from 870 nm (GaAs) to the near infrared (IR) range (1700 nm for GaSb) and thus has applications in the optical telecommunication industry, near IR light sensing, and thermovoltaics.²² In addition, it is an advantageous candidate for advanced band structure engineering as it can form a variety of band alignments (type I, II or III) with other common III–V compounds. In planar structures the $\text{InP}/\text{GaAs}_{0.51}\text{Sb}_{0.49}$ material system has resulted in double heterostructure bipolar transistors (DHBT) with the world record cut-off frequency of 700 GHz.²³ III–V NWs are considered as versatile building blocks for future optoelectronic applications due to their efficient strain relaxation, superior optical and electrical properties.²⁴ However, only

^aDepartment of Electronic Materials Engineering, Research School of Physics & Engineering, The Australian National University, Canberra, ACT 0200, Australia.
E-mail: xiaoming.yuan@anu.edu.au, philippe.caroff@anu.edu.au

^bCentre for Advanced Microscopy, The Australian National University, Canberra, ACT 0200, Australia

[†] Electronic supplementary information (ESI) available. See DOI: [10.1039/c4nr06307d](https://doi.org/10.1039/c4nr06307d)

a few reports on $\text{GaAs}_{1-x}\text{Sb}_x$ NWs have been published,^{4–6,25} with no work on controlling its composition, morphology and crystal structure. In GaSb and other Sb containing systems, it is shown that NW growth critically depends on the growth conditions, including small variations of the local environment.^{26,27} Sb is known to have a surfactant effect and has been utilized to alter crystal growth in planar layers.^{28,29} In the context of NWs, adding Sb in the vapour during Si NWs growth has been shown to suppress the VLS growth³⁰ while exposure of Au colloids treated $\text{GaAs}(111)\text{B}$ substrates to trimethylantimony prior to NW growth modifies the droplet/substrate wetting configuration.²⁶ Indeed, the exact role of Sb during NWs growth is still far from well understood.

Here we present our results on the growth of $\text{GaAs}_{1-x}\text{Sb}_x$ NWs and explain their morphology, crystal structure, composition and kinking behaviour. This allows us to tune their crystal properties towards application-ready NWs. Because temperature affects adatom diffusion length, precursor decomposition efficiency and also the effective V/III ratio simultaneously in metalorganic vapour phase epitaxy (MOVPE), this parameter is difficult to readily interpret and was therefore fixed in this study. All samples were grown at an optimal temperature of 500 °C, chosen after an initial screening process. $\text{GaAs}_{1-x}\text{Sb}_x$ NWs were grown on GaAs NW stems since they provided a clean interface decoupled from the substrate, allowing studies of the nucleation of $\text{GaAs}_{1-x}\text{Sb}_x$ by transmission electron microscopy (TEM) in a straightforward way.

2. Experimental details

NWs growth was carried out in a horizontal flow MOVPE reactor (Aixtron 200/4) at 100 mbar with a total gas flow rate of 15 litres per minute. Trimethylgallium (TMGa), trimethylantimony (TMSb) and arsine (AsH_3) were used as precursors for Ga, Sb and As, respectively. Au particle preparation was done by depositing 50 nm Au colloids on poly-L-lysine (PLL) treated $\text{GaAs}(111)\text{B}$ substrates.³¹ The substrates were then loaded into the reactor immediately and annealed at 600 °C for 10 min under AsH_3 ambient to desorb surface contaminants. The temperature was then cooled to 500 °C to initiate the growth of GaAs stems for 12 min. Growth of $\text{GaAs}_{1-x}\text{Sb}_x$ segment was initiated by introducing TMSb, and maintained for 90 min. In this study, the total precursor flow, AsH_3/TMGa and TMSb/TMGa ratios were considered as three independent parameters. A reference growth condition was defined as the following: $\text{TMGa} = 1.2 \times 10^{-5}$ mol min⁻¹ (III_0), $\text{AsH}_3/\text{TMGa} = 0.75$ and $\text{TMSb}/\text{TMGa} = 0.75$. Sb composition ratio in the nanowire

and vapour is defined as $\text{Sb}/(\text{As} + \text{Sb})$ and $\text{TMSb}/(\text{AsH}_3 + \text{TMSb})$, respectively. Under the reference growth condition all the $\text{GaAs}_{1-x}\text{Sb}_x$ NWs are vertical and have a twin-free zinc blende (ZB) structure. For clarity, the growth conditions for all the samples grown in this study are summarized in Table 1.

The morphology of all NWs was characterized using a Zeiss Ultraplus field emission scanning electron microscope (SEM) operating at 5 kV. NW crystal structure and composition information were determined by TEM and scanning transmission electron microscopy (STEM) using a JEOL2100F operated at 200 keV equipped with an energy-dispersive X-ray (EDX) spectroscopy. NW TEM samples were prepared by gentle mechanical transfer to a lacey carbon copper grid. Cross section samples were prepared using an ultra-microtomy method.¹³ Sb concentration was evaluated using the standard *K*-factor method.³² Twin-free ZB GaAs and GaSb nanowires of various diameters were used as reference samples to determine the diameter-dependent *K*-factors of As and Sb signal to extract the chemical composition from the EDX line scan. The calibrated *K*-factors of As and Sb using different reference nanowire diameters are shown in the ESI (Fig. S1†).

3. Morphology, composition and crystal structure tuning with growth conditions

3.1 Reference growth condition

Fig. 1 illustrates the key information, including morphology, crystal structure and 3-dimensional composition distribution for the reference $\text{GaAs}_{1-x}\text{Sb}_x$ nanowire sample. The GaAs stem is structurally quite defective, as expected for the growth temperature used, and covered with significant $\text{GaAs}_{1-x}\text{Sb}_x$ overgrowth, as shown in Fig. 1a. $\text{GaAs}_{1-x}\text{Sb}_x$ nanowires grow with a near 100% vertical yield and show some tapering. The crystal structure of a typical NW is twin-free ZB as depicted in Fig. 1b. This is consistent with previous studies of Sb-related NWs,^{10,25,26,33} which all reported a ZB structure. In addition to the crystal structure, the Sb content/distribution in the NWs is another important factor that may reveal the growth process and affect their optical properties. However, the composition evolution could be rather complex, especially when the NWs show tapering, because spontaneous core and shell formation is common in ternary NWs and their growth are governed by different mechanisms and hence resulting in different Sb incorporation.^{13,34} EDX analyses of both mechanically transferred nanowires and cross section samples were performed

Table 1 Summary of the growth conditions discussed in this work

	Fixed condition	#1	#2	#3	#4	#5	#6	#7	#8
AsH_3/TMGa series									
TMSb/TMGa	$\text{TMSb}/\text{TMGa} = 0.75$	0.5	1.5	2.5					
Precursor flow, $\times \text{III}_0$	$\text{AsH}_3/\text{TMGa} = 0.75$				0.5	1	1.5		
	$\text{AsH}_3/\text{TMGa} = 1.5$							0.5	1
	$\text{TMSb}/\text{TMGa} = 1.5$								

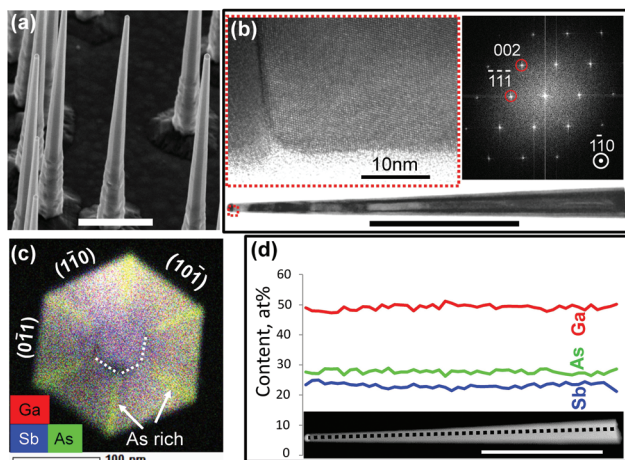


Fig. 1 Morphology, crystal structure and compositional profile of a typical $\text{GaAs}_{1-x}\text{Sb}_x$ NW sample. (a) 45° tilted SEM images. (b) Bright field TEM image of a NW along [1-10] zone axis with high resolution TEM image and the corresponding fast fourier transform (FFT), showing ZB twin-free structure. (c) EDX mapping of a cross section sample. Six As-rich bands along the $<112>$ corners in the shell could be seen. (d) EDX line scan along the same NW in (b) shows the uniformity of atomic composition along the length of the NW. Scale bars for (a), (b) and (d) are 1 μm .

to reveal the Sb profile. Fig. 1c shows the cross section composition mapping of the $\text{GaAs}_{1-x}\text{Sb}_x$ NW. An unintentionally formed core/shell structure is observed with the boundary indicated by the dashed line. Both core and shell have a hexagonal shape with predominantly {110} facets. In contrast, a 30° rotation could be seen between the GaAs core and overgrown $\text{GaAs}_{1-x}\text{Sb}_x$ shell on the GaAs stem (see Fig. S2 in the ESI†). The Sb content difference between the core and shell is around 0.06 with larger Sb in the core (Fig. 1c). Compared with Ga-seeded $\text{GaAs}_{1-x}\text{Sb}_x$ nanowires,⁶ our nanowire sidewalls are more regular (no significant micro-faceting or inverted tapering) and there is no atomic segregation at the core/shell interface. Phase segregation with six As-rich bands along the $<112>$ directions in the shell is identified in Fig. 1c (see arrows). Quantitatively, the As content along these bands is around 12% higher than the As content in the shell. Phase segregation for ternary shell growth has been commonly observed.^{12,13,35,36} An explanation based on anisotropic properties of crystal facets and diffusion length of adatoms has been proposed.^{11,36} The chemical potential of {112} facets being larger than {110} facets,³⁶ As and Sb adatoms are able to diffuse from {112} facets to {110} facets. Sb diffusion length could reach around 500 nm which is larger than that of As.^{27,37} Therefore, As-rich bands are formed along the six $<112>$ directions.

EDX line scan along the NW is shown in Fig. 1d. The measured Sb concentration is overall uniform along the length of the NW with slightly higher Sb at the tip than the base, despite its tapered morphology. In addition, the unchanged composition distribution indicates that diffusion-induced composition gradient in $\text{In}_{1-x}\text{Ga}_x\text{As}$ NWs along the axial direction³¹ is not significant here. Note that in comparison, $\text{GaAs}_{1-x}\text{Sb}_x$ segments or NWs grown by MBE^{6,38} show an increase of

the Sb concentration along the NW growth direction, which has been attributed to an As–Sb exchange reaction.³⁹

It is worth mentioning that due to tapering and composition difference between the core and shell is expected to cause a slight decrease of Sb content from the tip to the base of NW, around 2 atomic (at) % difference in Fig. 1d, because the Ga signal contributes to the other 50% of the total signal. However this very small variation is not clearly visible in Fig. 1d. This is explained by a combination of experimental uncertainty and slight wire-to-wire variability. Indeed, even when the EDX error is reduced to around 2 at% (estimated from the fluctuation of Ga content in Fig. 1d) by careful calibration of the *K*-factor in this work, the small Sb (and As) composition difference along the length of the NW may not be clearly observable from the EDX experiment in Fig. 1d. In addition, NW composition was found to vary slightly from wire-to-wire. In the Fig. S3,† EDX line scan results of another NW show that Sb content decreases around 2 at% from the tip to the base of NW, which agrees with our EDX analysis of the cross section sample. The above analysis indicates that the slight Sb variation along the NW comes from the Sb composition difference between the core and shell. In contrast, the Sb composition profile in the core is reasonably uniform along the NW.

Having described the main feature of a reference sample, we now turn to understanding the evolution of the NW morphology, crystal structure and composition with growth parameters.

3.2 AsH_3/TMGa ratio

To quantify the morphology of the NWs, we measured the axial growth rate and tapering ratio (TR), which are defined as: total length of the $\text{GaAs}_{1-x}\text{Sb}_x$ NW divided by the growth time, and diameter difference between the bottom and top divided by the $\text{GaAs}_{1-x}\text{Sb}_x$ NW length, respectively. Since no composition variation is detected from the EDX line scan along the growth direction of NW, only the overall Sb composition is presented based on the EDX analysis of at least ten NWs for each growth parameter. AsH_3/TMGa range is varied from 0.5 to 2.5 by increasing only the AsH_3 flow. The representative morphology, composition and structure change are shown in Fig. 2. In Fig. 2a, the $\text{GaAs}_{1-x}\text{Sb}_x$ NWs are short and quite tapered. In addition, around 14% of the NWs are kinked at large AsH_3 flow (sample #3, $\text{AsH}_3/\text{TMGa} = 2.5$), as indicated by the arrow. Neither the growth rate nor the TR changes much with increasing AsH_3 flow. TR is about 5% for the whole investigated range (Fig. 2b). NW growth rate remains fairly constant at around 35 nm min^{-1} when AsH_3/TMGa is below 1.5 but increases to about 53 nm min^{-1} at a ratio of 2.5. Interestingly, in contrast to the morphology, the Sb content in the NWs reduces significantly from 0.6 to 0.09 (Fig. 2b) when the Sb composition ratio in the vapour drops from 0.6 to 0.23 (when AsH_3 flow is increased). Sb incorporation into the NWs is larger at small AsH_3 flow and becomes significantly smaller at larger AsH_3 flow, suggesting that As is easier to precipitate from the Au seeds as compared to Sb, especially when there is

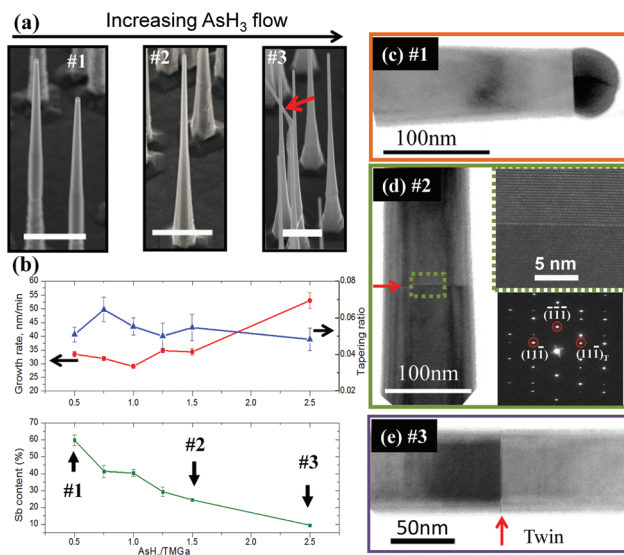


Fig. 2 Influence of AsH_3/TMGa ratio on the morphology, composition and crystal structure of $\text{GaAs}_{1-x}\text{Sb}_x$ NWs. (a) SEM images of NWs with various AsH_3/TMGa ratios: 0.5 (sample #1), 1.5 (sample #2) and 2.5 (sample #3). (b) Dependence of growth rate, tapering ratio and Sb content on AsH_3/TMGa ratio. TEM images of the samples #1 (c), #2 (d) and #3 (e) with arrow indicating the twin position. Inset in (d) is the SADP at the twin and corresponding HRTEM image. Scale bar and tilt angle in all SEM images are 1 μm and 45°, respectively.

enough As. The reason for this preferential nucleation is ascribed to the smaller formation energy of GaAs than that of GaSb.⁴⁰ As a consequence, Sb content in the NW is strongly dictated by AsH₃ flow.

Generally, Sb-related III-V NWs have a ZB structure and are mostly free of planar defects.^{6,10,41–43} In $\text{InAs}_{1-x}\text{Sb}_x$ NWs, a dependence of the density of planar defects on Sb composition has been reported, where NWs grow entirely twin-free above an Sb concentration threshold of 0.12.¹⁰ A similar trend is found here for the Au-seeded $\text{GaAs}_{1-x}\text{Sb}_x$ NWs and in the literature for the self-seeded $\text{GaAs}_{1-x}\text{Sb}_x$ NWs.⁶ Sample #1 is grown without any twins, as depicted in Fig. 2c. In sample #2, twins are visible in the bright field TEM image (Fig. 2d). The insets show a selected area diffraction pattern (SADP) and the corresponding high resolution transmission electron microscopy (HRTEM) image which confirm the presence of rotational twins. Twins can also be found in sample #3 (Fig. 2e). The formation of twins is controlled by AsH₃ flow, or more fundamentally, by the Sb content in the NW. It is observed that completely twin-free NWs are found for Sb concentration at or above 0.4 (AsH₃/TMGa below 1), while a few twins are observed below 0.4. Compared with $\text{InAs}_{1-x}\text{Sb}_x$, the threshold of Sb content is much higher in $\text{GaAs}_{1-x}\text{Sb}_x$ NWs. No clear variation of twin defect density is observed for the NWs with Sb concentration in the range of 0.09 to 0.29.

The AsH₃ flow has a moderate effect on the morphology of NWs but strongly affects the Sb content and formation of twins in the NWs. The kinking of the NWs (see red arrow in Fig. 2(a), sample #3) will be discussed in section 4.

3.3 TMSb/TMGa ratio

The effect of TMSb/TMGa ratio was studied by changing the TMSb flow while keeping the AsH₃/TMGa ratio constant at 0.75. As seen in Fig. 3 and in contrast to section 3.2 on the effect of AsH₃/TMGa ratio, the NWs morphology depends critically on TMSb flow. The NWs are vertical but quite tapered and short (sample #4) at low TMSb flow. Non-vertical NWs start appearing at higher TMSb flows. About 16% of the NWs are non-vertical (sample #5) and nearly none of the NWs are vertical when the TMSb/TMGa ratio is 1.5 (sample #6). Ignoring the non-vertical nature of the NWs, a clear trend of faster axial growth rate and reduced tapering is observed with increasing TMSb flow. More precisely, the NW growth rate triples from 12 nm min⁻¹ (sample #4) to 39 nm min⁻¹ (sample #5) and then increases further to 45 nm min⁻¹ (sample #6) when TMSb/TMGa ratio is increased from 0.5 to 1.0 to 1.5. At the same time, TR drops from 12% to around 3% in this range, which is ascribed to a combination of higher axial growth rate and reduced lateral growth rate. We also note that binary GaSb nanowires grown under similar conditions are perfectly taper-free (see ESI, Fig. S4a†). Therefore, it is suggested that lateral growth and tapering is controlled by Sb. TMSb could suppress the lateral growth rate. At low TMSb flow, lateral growth is large and the NWs are quite tapered while lateral growth rate is much smaller at high TMSb flow. In contrast to the change of morphology, the Sb content does not change substantially with TMSb in this range (see bottom

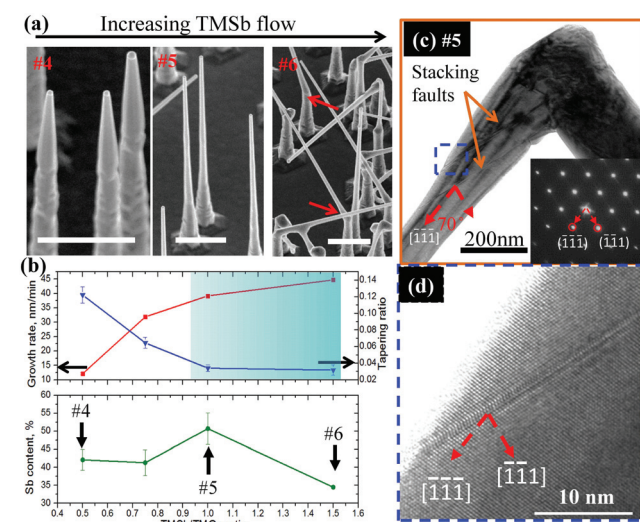


Fig. 3 Influence of TMSb/TMGa ratio on the morphology, composition and crystal structure of $\text{GaAs}_{1-x}\text{Sb}_x$ NWs. (a) SEM images of NWs with various TMSb/TMGa ratios: 0.5 (sample #4), 1 (sample #5) and 1.5 (sample #6). (b) Dependence of growth rate, tapering ratio and Sb content on the TMSb/TMGa ratio. (c) TEM image of a non-vertical NW in sample #5 shows the existence of inclined stacking faults. Inset is the corresponding SADP taken from the kinked part of the NW with inclined faults. (d) HRTEM image of the stacking faults marked in (c). Scale bar in SEM images is 1 μm . The cyan region in (b) indicates the condition where non-vertical NWs exist. The deeper the colour, the higher percentage of non-vertical NWs.

graph in Fig. 3b). Before the NWs become completely non-vertical, the Sb concentration increases only slightly from 0.42 to 0.51. In sample #6 where all the NWs are non-vertical, Sb content is now found to be smaller (0.35).

In terms of crystal structure, the twin defects observed previously (as a function of AsH_3/TMGa ratio) are now absent. Instead, another kind of planar defect, inclined fault, is found when the TMSb flow is relatively high (both in samples #5 and #6). The orange arrow in Fig. 3c shows an example of such an inclined fault in sample #5. The angle difference between the growth direction of the kinked NW and the normal to the plane of inclined faults, as indicated by the dotted red arrows in Fig. 3c, is measured to be 70° in agreement with the calculated angle between the $(-1 - 1 - 1)$ and $(-1 - 11)$ planes. This suggests that the inclined faults are in the $(-1 - 11)$ plane as confirmed by the corresponding SADP in the inset taken from the kinked part of the NW with inclined faults. Instead of clean twin diffraction spots, consecutive spots along $[-1 - 11]$ direction are observed from the inset SADP, indicating that the planar defects are stacking faults. HRTEM image (see Fig. 3d) of this region marked by a dotted box in Fig. 3c shows a combination of stacking faults and a thin twinned region of a few bilayers. In addition to kinked NWs, inclined faults are also found in vertical NWs (sample #5) but mostly at the bottom of the $\text{GaAs}_{1-x}\text{Sb}_x$ NWs, while the top part has a twin-free ZB structure. These inclined faults, either twins or stacking faults, have been recently associated with kinking phenomena in semiconductor NWs.^{44–46} Hocevar *et al.*⁴⁴ pointed out that Au alloy droplet may move to wet the sidewall and form inclined facets when growing Si NWs on GaP stems due to reduced surface energy of the droplet. Then nucleation could happen at the inclined facets resulting in the formation of inclined faults. Similarly here, kinked NWs are caused by the inclined faults, which we attribute to a decrease in the surface energy of Au alloy particle (liquid–vapour surface) when the TMSb flow is high. The role of TMSb is related to the surfactant property of Sb as will be further discussed later. Similar case can also be observed for GaSb NWs. Indeed GaSb NWs can crawl around the GaAs stems at high TMSb flow rates (see ESI Fig. S4b†).

3.4 Total flow of group III and V precursor

In addition to AsH_3/TMGa and TMSb/TMGa ratios, the total flow of the precursors (both group III and V flows) at a fixed V/III ratio also affects $\text{GaAs}_{1-x}\text{Sb}_x$ NWs growth. The results obtained for varying TMGa flow with both AsH_3/TMGa and TMSb/TMGa ratios fixed at 1.5 are shown in Fig. 4. As indicated in Fig. 4a, the morphology of $\text{GaAs}_{1-x}\text{Sb}_x$ NWs is sensitive to TMGa flow rate. At a low flow rate, the NWs are all vertical and slightly tapered (sample #7). However, the NWs grow faster but are nearly all kinked at a high flow rate (sample #8). A sharp drop of TR is observed for a slight increase of flow rate from 0.5III_0 to 0.75III_0 , which is ascribed to the largely suppressed lateral growth rate at high precursor flow. Further increase of precursor flow does not change TR due to the already nearly taper free morphology but only improve the

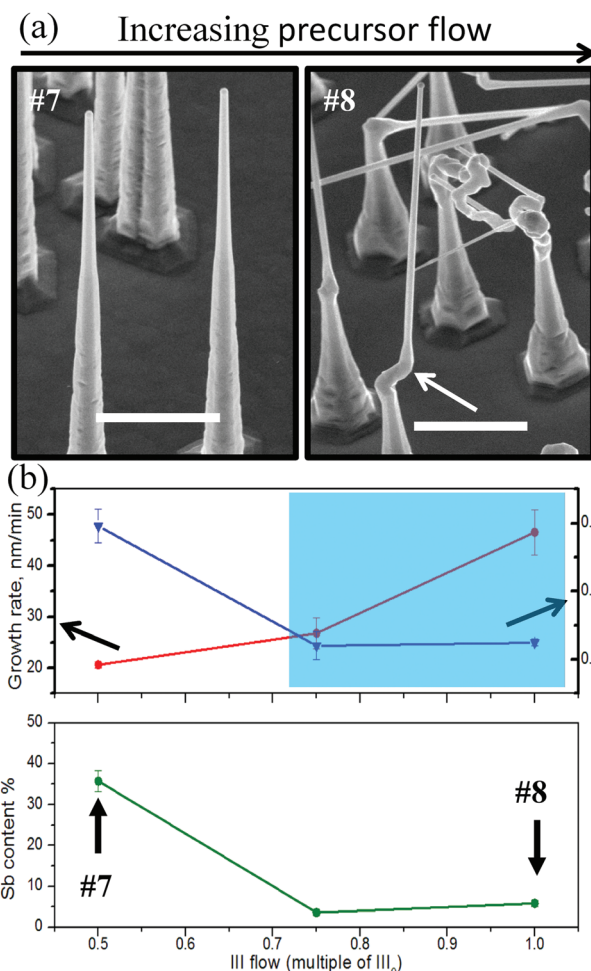


Fig. 4 Influence of precursor flow rate, with both AsH_3/TMGa and TMSb/TMGa ratios fixed at 1.5, on the morphology and composition of $\text{GaAs}_{1-x}\text{Sb}_x$ NWs. (a) SEM images of NWs with two different III flows: 0.5 (sample #7) and 1 (sample #8). (b) Dependence of growth rate, tapering ratio and Sb content on the group III flow. Scale bar in SEM images is 1 μm . The cyan region in (b) indicates the condition where non-vertical NWs exist.

axial growth rate along the kinked direction. The Sb content depends critically on the precursor flow. It is as high as 0.35 at low flow rate (0.5III_0) but decreases drastically to stabilize around 0.04 at high flow rate (see bottom graph in Fig. 4b). Inclined faults are also observed in kinked NWs but all NWs have a ZB twin-free structure.

As one would expect, the effect of total precursor flow rate on the morphology of $\text{GaAs}_{1-x}\text{Sb}_x$ NWs also depends on the AsH_3/TMGa and TMSb/TMGa ratios. When both AsH_3/TMGa and TMSb/TMGa ratios are small and fixed at 0.75 (see the results in Fig. S5 in the ESI†), only about 17% of the NWs are non-vertical at 2III_0 (see Fig. S5†) while nearly all the NWs are kinked at 0.75III_0 when AsH_3/TMGa and TMSb/TMGa ratios are fixed at 1.5 (see Fig. 4). These results demonstrate a delicate balance of flow rate, the AsH_3/TMGa and TMSb/TMGa ratios is required to control the morphology of $\text{GaAs}_{1-x}\text{Sb}_x$ NWs. In addition, inclined faults are found in vertical NWs

grown at high flow rates. Fig. S5e–g in the ESI† shows an example of that delicate balance being compromised, with the Au catalyst located on the side facet at the top of the NW while inclined defects are visible at the base of the $\text{GaAs}_{1-x}\text{Sb}_x$ NW. This provides evidence that Au seed could be pushed to wet the sidewall during NW growth, resulting in crawling or kinking. Or alternatively, if the Au seed manages to re-pin itself on the top, the NWs could continue to grow vertically, leaving with some residual inclined faults as a result.

In this section, we have investigated the role of AsH_3/TMGa and TMSb/TMGa ratios, and the total precursor flow rate on the morphology, composition and crystal structure of $\text{GaAs}_{1-x}\text{Sb}_x$ NWs. In terms of morphology, NW growth features can be discussed in terms of tapering (lateral growth), axial growth and kinking. Lateral growth can be tuned by changing TMSb flow. At large TMSb flows (either higher TMSb/TMGA ratio or higher total precursor flow), Sb could cover the sidewall of NWs due to its surfactant effect,⁴⁷ and suppress the nucleation of $\text{GaAs}_{1-x}\text{Sb}_x$ on the sidewall. Consequently, tapering is reduced and nearly taper-free NWs can be achieved for a given set of growth parameters (sample #8). No obvious change of tapering is observed by changing AsH_3 flow. Increasing total precursor flow or TMSb/TMGA ratio improves the axial growth rate by increasing its driving force (supersaturation). At high TMSb flow, reduced lateral growth pushes more Ga, As and Sb adatoms into the Au catalyst, which increases axial growth. In comparison, the variation of axial growth rate with AsH_3 flow is not as sensitive as TMSb flow. NW kinking is ascribed to the higher TMSb flow, either at high TMSb/TMGA ratio or total precursor flow. Kinked NWs are also observed at much larger AsH_3 flow which is ascribed to an increase of Sb content in the Au due to the decrease of Sb incorporation ratio at higher AsH_3 flow. From the above analysis, high TMSb flow is required to achieve taper-free $\text{GaAs}_{1-x}\text{Sb}_x$ NWs. However the NWs are very likely to grow non-vertically, either kinked or bent, at these high flow rate conditions. Temperature, which is an important factor, is fixed on purpose in this study but could be changed to influence further the NW morphology.

In contrast, the Sb content in the NW decreases with increasing AsH_3 flow while the Sb content variation with TMSb flow is not substantial. This could be due to As adatoms combining more readily with Ga adatoms to form a GaAs crystal. In addition, an unexpected drop in Sb content is observed with increasing TMSb/TMGA ratio (see sample #6 in Fig. 3) or total precursor flow (see sample #8 in Fig. 4), which appears counter-intuitive. A tentative explanation for this growth behavior is proposed as follows. As TMSb flow is increased in the vapor, it also covers the NW sidewalls, drastically reducing lateral overgrowth (reducing tapering and volume of shell material, as measured and clearly visible in Fig. 3), thereby freeing-up As adatoms that can serve as a secondary source and increasing the As concentration in the droplet as a result. Note that this group V secondary source mechanism has been unambiguously demonstrated in a work on self-seeded GaAs nanowires.³⁷ We show in Fig. 2. that it is the As concentration in the droplet that controls the Sb composition in the NW,

therefore high TMSb flow leads to low Sb concentration in the NW because it indirectly leads to an As-rich droplet.

$\text{GaAs}_{1-x}\text{Sb}_x$ NWs grown at various conditions show a pure ZB structure with two kinds of planar defects: normal twins in vertical NWs and inclined faults in most non-vertical NW. For the first type of defects, twin defects are found to depend on the AsH_3 flow or Sb content in the NWs. Sb content needs to reach nearly 0.4 to form a twin-free ZB structure (with $\text{TMSb}/\text{TMGa} = 0.75$, $\text{TMGa} = 1.2 \times 10^{-5} \text{ mol min}^{-1}$). It is found that this threshold also depends on the TMSb/TMGa ratio and precursor flow rate. At higher TMSb flow, $\text{GaAs}_{1-x}\text{Sb}_x$ NWs with only 4 percent of Sb can also form a twin-free structure. In comparison both high TMSb/TMGa ratio and total precursor flow result in inclined faults in kinked NWs. Understanding the formation of inclined faults and its relation with kinked NWs is important and is thus discussed in the next section.

4. Understanding of inclined faults in non-vertical NWs

During axial heterostructure growth, it has been proposed that NW kinking and crawling is a result of island formation at the interface of the heterostructure due to reduced interface energy.^{48,49} In this hypothesis, an island instead of a layer is formed since from thermodynamics consideration, the Au particle is unlikely to wet the newly formed nuclei. Island formation then pushes the Au particle to the side of the NW, leading to kinking or crawling. Accordingly, a compositionally graded layer will reduce the nucleation barrier for layer growth and avoid island formation. To test this hypothesis, a graded layer was grown between GaAs and $\text{GaAs}_{1-x}\text{Sb}_x$ under the growth conditions of sample #8. The graded layer first starts with the condition of the reference sample for 3 min and then gradually increased to the growth condition of sample #8 over 5 min in order to remove the nucleation barrier and minimize lattice and surface energy difference between each layer. However, no improvement of the vertical NWs yield is observed using this procedure (Fig. S6 in the ESI†). Therefore, non-vertical NWs are not due to an abrupt change of the growth conditions but the steady-state growth condition itself is also not favoring vertical NW growth. Besides, this hypothesis also cannot explain the existence of inclined defects found in non-vertical NWs. Instead, inclined faults and kinking can be a result of the change in surface energy. Fig. 5(a) shows a schematic of a Au-seeded NW with the wetting angle and surface energies defined at the triple phase line. γ_{LS} , γ_{SV} and γ_{LV} are the surface energy of liquid-solid, solid-vapour and liquid-vapour interface, respectively. For steady NW growth, the wetting angle θ should satisfy Young's equation: $\cos \theta = -\gamma_{LS}/\gamma_{LV}$. Besides, θ should be within a range of angles to satisfy the criterion deduced by Nebol'sin.⁵⁰ During NW growth in the presence of a surfactant, for instance Sb, surface energies at the growth front could be substantially altered. An evidence of the change in surface energy can be inferred from the wetting angle difference of the Au droplet. Even though the measured

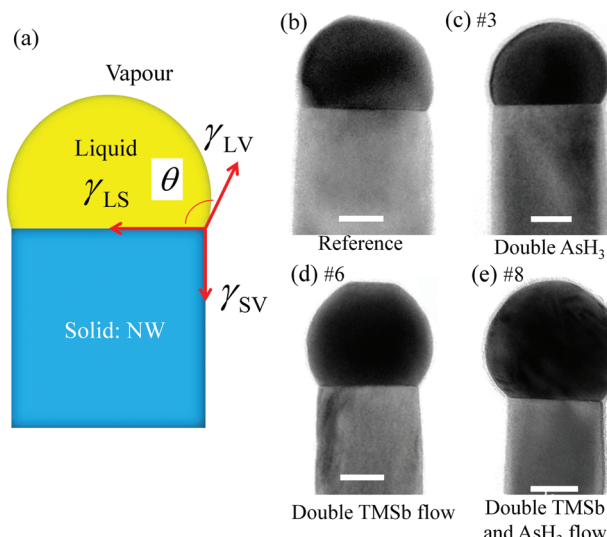


Fig. 5 Au droplet configuration after growth, showing the increase of wetting angle with high TMSb flow. (a) Schematic of the surface energy and configuration of the Au droplet. (b–e) bright field TEM images of the Au catalyst along [1–10] zone axis: reference sample (b), double AsH_3 flow (c), double TMSb flow (d) and double both TMSb and AsH_3 flows (e). Scale bar is 20 nm.

wetting configuration after growth and during growth could be different, the results can still provide an insight into the growth mechanism as discussed below.

Fig. 5(b)–(e) compare the effect of AsH_3 and TMSb flow rates on the wetting angle. For direct comparison, the contact angles of the NWs are all measured from TEM images oriented along the [1–10] zone axis. For the sample grown with the reference condition, θ lies in the range of 95–110° (Fig. 5b). Only a slight increase in θ is observed when doubling the AsH_3 flow (Fig. 5c). In contrast, if TMSb flow is doubled, θ increases to around 120° (Fig. 5d) and is further increased to about 130° (Fig. 5e) as both AsH_3 and TMSb flows are doubled. All NWs in Fig. 5b and c are vertically oriented while most NWs are non-vertical in Fig. 5d and e. When the cooling down conditions of the above four samples are changed to be the same as that of sample #8 (double AsH_3 and TMSb flow), the observed change in θ is very similar to the results presented in Fig. 5 (see Fig. S7 in the ESI†). It indicates that the measured wetting configuration is not much affected by the cooling down conditions and could represent the real situation during growth. Increase of θ at high TMSb flow is related to the increase of $\gamma_{\text{LS}}/\gamma_{\text{LV}}$, either by a reduction in γ_{LV} or an increase in γ_{LS} . Since the liquid-vapour surface is directly exposed to the vapour phase and Sb is known to reduce surface energy because of its surfactant role, a drop of γ_{LV} is expected. EDX analysis shows the presence of Ga in the Au particle for all the four samples. Noticeable amount of Sb is only found in sample #8 (Fig. 5e) and sometimes even AuSb_2 phase is observed in the seed alloy. Ga (0.72 J m^{-2}) and Sb (0.366 J m^{-2}) have a smaller surface energy than Au (1.14 J m^{-2}), thus could result in the change of wetting angle.^{47,51} Ga concentration in the Au alloy for the

reference sample (Fig. 5b) and sample #6 (Fig. 5d) is similar with an averaged concentration around 50 at% while the wetting angle difference is substantial. This indicates that Ga content in the Au alloy is not critical in determining the wetting configuration in the present case. Eliminating these possibilities, Sb is ascribed to be the reason for the change in surface energy and the increase in θ due to its surfactant effect. As TMSb flow is increased, γ_{LV} is reduced, resulting in a corresponding increase in θ . With the reduction of γ_{LV} , the allowed θ range for NW growth becomes smaller and the tendency for the Au seed moving to the sidewall increases. As the Au seed moves to the NW sidewall and forms an inclined facet (see Fig. S7d†), nucleation can now occur at the inclined interface. As a result, inclined faults could form, leading to NW kinking and even forming curved NWs.⁴⁴ This explains why $\text{GaAs}_{1-x}\text{Sb}_x$ and GaSb NWs growth is extremely sensitive to TMSb flow.

To further understand the formation of inclined faults, $\text{GaAs}_{1-x}\text{Sb}_x$ NWs were grown for only 5 min with the same condition as that of sample #8 (double AsH_3 and TMSb flow). As seen in Fig. 6a, both vertical and non-vertical NWs are observed. If the growth time is extended to 7.5 min, nearly all the NWs kink or bend. These observations indicate that $\text{GaAs}_{1-x}\text{Sb}_x$ NWs are not kinked or bent immediately following the switch from GaAs stem to $\text{GaAs}_{1-x}\text{Sb}_x$ NW growth, which is in contrast to the proposed mechanism of kinking induced by island formation.⁴⁸ In addition, both $\text{GaAs}_{1-x}\text{Sb}_x$ NWs and Au particles have irregular shape, indicating the crystal growth is more complex than layer-by-layer growth model for NWs. TEM image along with EDX line scan in Fig. 6b demonstrates the formation of inclined faults after around 60 nm of straight

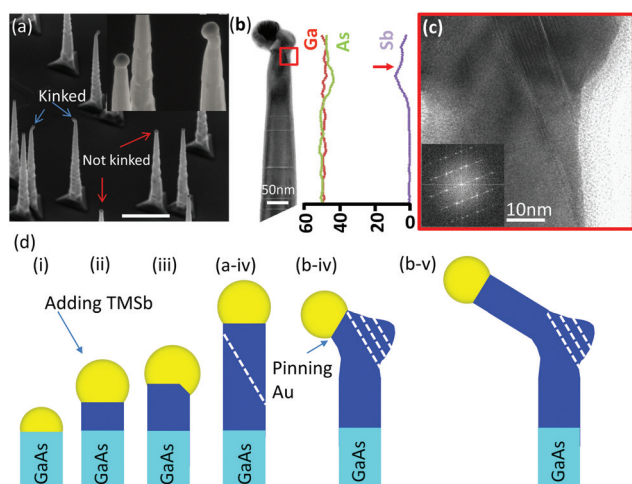


Fig. 6 The formation of inclined defects and a schematic of non-vertical NWs. (a) SEM of $\text{GaAs}_{1-x}\text{Sb}_x$ grown only for 5 min, showing the vertical and non-vertical NWs. (b) TEM/EDX of a curved NW with inclined defects. Arrow indicates the position of inclined faults. (c) HRTEM image of the marked region in (b). Both twins and stacking faults could be observed. The inset FFT shows the spots as a result of twins and streaking as a result of stacking faults. (d) Schematic showing the evolution of non-vertical NWs with inclined defects. White dotted lines depicts inclined faults. Scale bar in (a) is 1 μm .

$\text{GaAs}_{1-x}\text{Sb}_x$ segment. This indicates that Au seeds need time to evolve from a stable growth configuration to wet the sidewall and form inclined faults. No Sb concentration difference is observed in the $\text{GaAs}_{1-x}\text{Sb}_x$ segment before and after the formation of inclined faults, which is around a few percents. Irregular shape of $\text{GaAs}_{1-x}\text{Sb}_x$ evolves after the formation of inclined faults, implying that the inclined faults are a “landmark” for unstable NW growth. A closer look reveals that the inclined faults contain both twins and stacking faults, as shown by the HRTEM image and FFT in Fig. 6c.

From the above information we propose a growth scenario for $\text{GaAs}_{1-x}\text{Sb}_x$ NWs growth as illustrated in Fig. 6d. After switching from GaAs to $\text{GaAs}_{1-x}\text{Sb}_x$, the NWs still grow somewhat in a stable mode while the wetting angle of Au particle starts to increase (ii). After sufficient Sb accumulation in the Au catalyst, the droplet becomes unstable and wet the sidewalls to form a {111} inclined interface (iii). Then the inclined interface becomes an alternative growth nucleation site and planar defects could develop at the inclined facet. After that, if the Au alloy seed “recovers”, a straight NW with inclined defects may form (a-iv). In other cases, as the Au droplet keeps moving, growth becomes unstable and increasingly complex resulting in the formation of twisted segments with a high density of defects (b-iv). As the Au seeds keep evolving, they could finally find a stable wetting configuration and results in kinked growth (b-v).

5. Summary and conclusion

In conclusion, we have successfully grown $\text{GaAs}_{1-x}\text{Sb}_x$ NWs with a wide range of Sb compositions from 0.08 to 0.6. A core/shell structure is spontaneously formed in tapered $\text{GaAs}_{1-x}\text{Sb}_x$ NWs with 6 As-rich bands along the six {112} directions, indicating the surface diffusion length of Sb is larger than that of As. The effect of growth parameters (AsH_3/TMGa , TMSb/TMGa and total precursor flow) on the morphology, composition and crystal structure is studied. AsH_3 flow is effective in tuning the composition of $\text{GaAs}_{1-x}\text{Sb}_x$ NWs ($x = 0.09\text{--}0.6$) while NW morphology is more sensitive to TMSb flow. In addition to high TMSb flow, high AsH_3 flow can cause NWs kinking by increasing Sb concentration in the Au due to lower Sb incorporation efficiency at high AsH_3 flow. Consequently, a delicate balance of the above growth conditions is required to avoid twin defects and NWs kinking. Inclined defects are found to be a “landmark” for kinked NWs. High Sb content in the Au induced by either high TMSb flow or reduced Sb incorporation efficiency reduces the surface energy at the liquid–vapour interface, γ_{LV} , making the wetting configuration unstable for NW growth, forming inclined faults and kinked NWs.

This study has revealed some fundamental phenomena that are general to all III–V ternary nanowires such as the competition for incorporation of one or more element(s) controlled by a single species (As in this case), crystal phase/composition intricacies, role of surfactants in anisotropic crystal growth, influence of growth parameters on tapering, and insights into

the fundamental reasons for kinking in nanowires. Moreover, these high quality tapered, twin free and composition tunable $\text{GaAs}_{1-x}\text{Sb}_x$ NWs are now ready for use in a broad range of infra-red applications.

Acknowledgements

The Australian Research Council is acknowledged for financial support. Access to facilities used in this work is made possible through the Australian National Fabrication Facility, ACT Node and Australian Microscopy and Microanalysis Research Facility.

Notes and references

- X. Zhuang, C. Z. Ning and A. Pan, *Adv. Mater.*, 2012, **24**, 13–33.
- S. Assali, I. Zardo, S. Plissard, D. Kriegner, M. A. Verheijen, G. Bauer, A. Meijerink, A. Belabbes, F. Bechstedt, J. E. M. Haverkort and E. P. A. M. Bakkers, *Nano Lett.*, 2013, **13**, 1559–1563.
- S. G. Ghalamestani, M. Ek, B. Ganjipour, C. Thelander, J. Johansson, P. Caroff and K. A. Dick, *Nano Lett.*, 2012, **12**, 4914–4919.
- D. L. Dheeraj, G. Patriarche, H. L. Zhou, T. B. Hoang, A. F. Moses, S. Gronsberg, A. T. J. van Helvoort, B. O. Fimland and H. Weman, *Nano Lett.*, 2008, **8**, 4459–4463.
- S. Plissard, K. A. Dick, X. Wallart and P. Caroff, *Appl. Phys. Lett.*, 2010, **96**, 121901.
- S. Conesa-Boj, D. Kriegner, X.-L. Han, S. Plissard, X. Wallart, J. Stangl, A. Fontcuberta i Morral and P. Caroff, *Nano Lett.*, 2014, **14**, 326–332.
- G. Koblmüller and G. Abstreiter, *Phys. Status Solidi RRL*, 2014, **8**, 11–30.
- S. Hertenberger, S. Funk, K. Vizbaras, A. Yadav, D. Rudolph, J. Becker, S. Bolte, M. Doblinger, M. Bichler, G. Scarpa, P. Lugli, I. Zardo, J. J. Finley, M. C. Amann, G. Abstreiter and G. Koblmüller, *Appl. Phys. Lett.*, 2012, **101**, 043116.
- D. Ercolani, G. Mauro, N. Lucia, R. Francesca, P. Marialilia, L. Ang, S. Giancarlo, B. Fabio and S. Lucia, *Nanotechnology*, 2012, **23**, 115606.
- T. Xu, K. A. Dick, S. Plissard, T. H. Nguyen, Y. Makoudi, M. Berthe, J.-P. Nys, X. Wallart, B. Grandidier and P. Caroff, *Nanotechnology*, 2012, **23**, 095702.
- M. Heiss, Y. Fontana, A. Gustafsson, G. Wüst, C. Magen, D. D. O'Regan, J. W. Luo, B. Ketterer, S. Conesa-Boj, A. V. Kuhlmann, J. Houel, E. Russo-Averchi, J. R. Morante, M. Cantoni, N. Marzari, J. Arbiol, A. Zunger, R. J. Warburton and A. Fontcuberta i Morral, *Nat. Mater.*, 2013, **12**, 439–444.
- Y.-N. Guo, T. Burgess, Q. Gao, H. H. Tan, C. Jagadish and J. Zou, *Nano Lett.*, 2013, **13**, 5085–5089.

- 13 Y.-N. Guo, H.-Y. Xu, G. J. Auchterlonie, T. Burgess, H. J. Joyce, Q. Gao, H. H. Tan, C. Jagadish, H.-B. Shu, X.-S. Chen, W. Lu, Y. Kim and J. Zou, *Nano Lett.*, 2013, **13**, 643–650.
- 14 S. K. Lim, M. J. Tambe, M. M. Brewster and S. Gradečak, *Nano Lett.*, 2008, **8**, 1386–1392.
- 15 P. K. Mohseni, A. Behnam, J. D. Wood, C. D. English, J. W. Lyding, E. Pop and X. Li, *Nano Lett.*, 2013, **13**, 1151–1161.
- 16 J. Xu, X. Zhuang, P. Guo, W. Huang, W. Hu, Q. Zhang, Q. Wan, X. Zhu, Z. Yang, L. Tong, X. Duan and A. Pan, *Sci. Rep.*, 2012, **2**, 820.
- 17 S. Sprengel, A. Andrejew, K. Vizbaras, T. Gruendl, K. Geiger, G. Boehm, C. Grasse and M.-C. Amann, *Appl. Phys. Lett.*, 2012, **100**, 041109.
- 18 G. Blume, K. Hild, I. P. Marko, T. J. C. Hosea, S.-Q. Yu, S. A. Chaparro, N. Samal, S. R. Johnson, Y.-H. Zhang and S. J. Sweeney, *J. Appl. Phys.*, 2012, **112**, 033108.
- 19 C. Baile, W. Y. Jiang, Y. Jinrong, A. L. Holmes and B. M. Onat, *IEEE Photonics Technol. Lett.*, 2011, **23**, 218–220.
- 20 S. Hatch, J. Wu, K. Sablon, P. Lam, M. Tang, Q. Jiang and H. Liu, *Opt. Express*, 2014, **22**, A679–A685.
- 21 H. Detz, J. Silvano de Sousa, H. Leonhardt, P. Klang, T. Zederbauer, A. M. Andrews, W. Schrenk, J. Smoliner and G. Strasser, *J. Vac. Sci. Technol., B*, 2014, **32**, 02C104.
- 22 L. Fraas, J. Avery, V. S. Sundaram, V. T. Dinh, T. M. Davenport, J. W. Yerkes, J. Gee and K. Emery, *Over 35% efficient GaAs/GaSb stacked concentrator cell assemblies for terrestrial applications*, 1990.
- 23 R. Flückiger, R. Lövblom, M. Alexandrova, O. Ostinelli and C. R. Bolognesi, *Appl. Phys. Express*, 2014, **7**, 034105.
- 24 R. Yan, D. Gargas and P. Yang, *Nat. Photonics*, 2009, **3**, 569–576.
- 25 D. L. Dheeraj, G. Patriarche, L. Largeau, H. L. Zhou, A. T. J. v. Helvoort, F. Glas, J. C. Harmand, B. O. Fimland and H. Weman, *Nanotechnology*, 2008, **19**, 275605.
- 26 B. M. Borg and L.-E. Wernersson, *Nanotechnology*, 2013, **24**, 202001.
- 27 S. R. Plissard, D. R. Slapak, M. A. Verheijen, M. Hocevar, G. W. G. Immink, I. van Weperen, S. Nadj-Perge, S. M. Frolov, L. P. Kouwenhoven and E. P. A. M. Bakkers, *Nano Lett.*, 2012, **12**, 1794–1798.
- 28 T. Matsuura, T. Miyamoto, T. Kageyama, M. Ohta, Y. Matsui, T. Furuhata and F. Koyama, *Jpn. J. Appl. Phys.*, 2004, **43**, L605.
- 29 A. Portavoce, I. Berbezier and A. Ronda, *Mater. Sci. Eng., B*, 2003, **101**, 181–185.
- 30 P. Nimmatoori, Q. Zhang, E. C. Dickey and J. M. Redwing, *Nanotechnology*, 2009, **20**, 6.
- 31 Y. Kim, H. J. Joyce, Q. Gao, H. H. Tan, C. Jagadish, M. Paladugu, J. Zou and A. A. Suvorova, *Nano Lett.*, 2006, **6**, 599–604.
- 32 D. B. Williams and C. B. Carter, *Springer science & Business Media*, 5 August 2009 edn., 2009, vol. 3, p. 760.
- 33 R. A. Burke, X. J. Weng, M. W. Kuo, Y. W. Song, A. M. Itsuno, T. S. Mayer, S. M. Durbin, R. J. Reeves and J. M. Redwing, *J. Electron. Mater.*, 2010, **39**, 355–364.
- 34 R. S. Wagner and W. C. Ellis, *Appl. Phys. Lett.*, 1964, **4**, 89–90.
- 35 C. Zheng, J. Wong-Leung, Q. Gao, H. H. Tan, C. Jagadish and J. Etheridge, *Nano Lett.*, 2013, **13**, 3742–3748.
- 36 J. B. Wagner, N. Sköld, L. Reine Wallenberg and L. Samuelson, *J. Cryst. Growth*, 2010, **312**, 1755–1760.
- 37 M. R. Ramdani, J. C. Harmand, F. Glas, G. Patriarche and L. Travers, *Cryst. Growth Des.*, 2012, **13**, 91–96.
- 38 D. L. Dheeraj, G. Patriarche, H. Zhou, J. C. Harmand, H. Weman and B. O. Fimland, *J. Cryst. Growth*, 2009, **311**, 1847–1850.
- 39 H. Kauko, B. O. Fimland, T. Grieb, A. M. Munshi, K. Müller, A. Rosenauer and A. T. J. van Helvoort, *J. Appl. Phys.*, 2014, **116**, 144303.
- 40 J. B. Li, W. Zhang, C. Li and Z. Du, *JPE*, 1998, **19**, 466–472.
- 41 Y. N. Guo, J. Zou, M. Paladugu, H. Wang, Q. Gao, H. H. Tan and C. Jagadish, *Appl. Phys. Lett.*, 2006, **89**, 231917.
- 42 P. Caroff, M. E. Messing, B. M. Borg, K. A. Dick, K. Deppert and L. E. Wernersson, *Nanotechnology*, 2009, **20**, 7.
- 43 S. Gorji Ghalamestani, M. Ek, B. Ganjipour, C. Thelander, J. Johansson, P. Caroff and K. A. Dick, *Nano Lett.*, 2012, **12**, 4914–4919.
- 44 M. Hocevar, G. Immink, M. Verheijen, N. Akopian, V. Zwiller, L. Kouwenhoven and E. Bakkers, *Nat. Commun.*, 2012, **3**, 1266–1266.
- 45 M. Zhang, F. Wang, C. Wang, Y. Wang, S. Yip and J. Ho, *Nanoscale Res. Lett.*, 2014, **9**, 211.
- 46 N. Jeon, S. A. Dayeh and L. J. Lauhon, *Nano Lett.*, 2013, **13**, 3947–3952.
- 47 R. Novakovic, D. Giuranno, E. Ricci, S. Delsante, D. Li and G. Borzone, *Surf. Sci.*, 2011, **605**, 248–255.
- 48 K. A. Dick, S. Kodambaka, M. C. Reuter, K. Deppert, L. Samuelson, W. Seifert, L. R. Wallenberg and F. M. Ross, *Nano Lett.*, 2007, **7**, 1817–1822.
- 49 M. Paladugu, J. Zou, Y.-N. Guo, G. J. Auchterlonie, H. J. Joyce, Q. Gao, H. Hoe Tan, C. Jagadish and Y. Kim, *Small*, 2007, **3**, 1873–1877.
- 50 V. A. Nebol'sin and A. A. Shchetinin, *Inorg. Mater.*, 2003, **39**, 899–903.
- 51 F. Glas, J.-C. Harmand and G. Patriarche, *Phys. Rev. Lett.*, 2007, **99**.